ROYAL SOCIETY OF CHEMISTRY

EDGE ARTICLE

CrossMark
click for updates

Asymmetric supercapacitors with high energy density based on helical hierarchical porous Na$_x$MnO$_2$ and MoO$_2$†

Xue-Feng Lu, Zhi-Xiang Huang, Ye-Xiang Tong and Gao-Ren Li*

Helical hierarchical porous Na$_x$MnO$_2$/CC and MoO$_2$/CC, which are assembled from nanosheets and nanoparticles, respectively, are fabricated using a simple electrodeposition method. These unique helical porous structures enable electrodes to have a high capacitance and an outstanding cycling performance. Based on the helical Na$_x$MnO$_2$/CC as the positive electrodes and helical MoO$_2$/CC as the negative electrodes, high performance Na$_x$MnO$_2$/CC//MoO$_2$/CC asymmetric supercapacitors (ASCs) are successfully assembled, and they achieve a maximum volume C_{sp} of 2.04 F cm^{-3} and a maximum energy density of 0.92 mW h cm^{-3} for the whole device and an excellent cycling stability with 97.22% C_{sp} retention after 6000 cycles.

1. Introduction

Increasing demands in portable electronics and future green transportation are pushing the research towards electrochemical energy storage (EES) systems with high energy density, high power density and long cycling life.[1] Electrochemical capacitors, also known as supercapacitors, bridge the gap between batteries and conventional capacitors in terms of their high power density and have been regarded as the most promising EES devices.[2] However, their energy density is still relatively low, which has restricted their potential applications. Therefore, the improvement of energy density is crucial for supercapacitors to meet future energy demands.

As we know, the energy density of a supercapacitor device can be calculated according to the equation $E = 1/2C_{sp}V^2$, and it can be enhanced by maximizing the specific capacitance (C_{sp}) and operation voltage (V).[3] The promising approach for the enhancement of C_{sp} is to develop new electrodes with high C_{sp} values.[4] An effective approach to increase the operation voltage is to use an organic electrolyte, which can provide a wide voltage window up to 3.0 V. However, they suffer from high cost, poor ionic conductivity and high toxicity, which limit their wide application. In addition, a promising alternative for increasing the operation voltage is to develop asymmetric supercapacitors (ASCs), which typically consist of cathodes as the energy source and anodes as the power source.[5] Compared with symmetric supercapacitors, the ASCs

take advantage of the different voltage windows of two electrodes in the same electrolyte to increase the device operating voltage and thus significantly improve the energy density. In recent decades, intensive efforts have been devoted to explore various ASCs, such as H–TiO$_2$@MnO$_2$//H–TiO$_2$@C (1.8 V),[4] ZnO@MnO$_2$//rGO (1.8 V),[6] Ni/NiO//rGO (1.5 V),[7] and NiCo$_2$O$_4$// active carbon (1.5 V).[8] Most ASCs use carbon-based materials as negative electrodes because of their large surface area, excellent electrical conductivity and outstanding stability.[9] However, the low C_{sp} of carbon materials severely limits the energy density of the SCs according to the equation of $1/C = 1/C_{an} + 1/C_{cat}$ (C_{an}: capacitance of the anode; C_{cat}: capacitance of the cathode). In this regard, some new negative electrodes with high C_{sp} values, such as MoO$_3$,[3a,10] Fe$_2$O$_3$,[11] and some metal nitrides[12] have been developed for ASCs. But due to the narrow voltage window, the unbalanced capacity between the cathode and anode electrodes and the unsatisfactory cycling stability of metal oxide negative electrodes, it is still a huge challenge to achieve ASCs with high energy and power densities.

Based on the above considerations, in this paper we designed and synthesized helical hierarchical porous Na$_x$MnO$_2$ and MoO$_2$ on carbon cloth (CC) as the positive and negative electrodes, respectively, for ASCs. Manganese oxides have been widely thought to be the most promising material because of their low cost, high abundance, large theoretical C_{sp}, and environmental friendliness.[13] As a polymorph of MnO$_2$, the sodium–birnessite-type MnO$_2$ (Na$_x$MnO$_2$) has a two-dimensional layer-structure with bicontinuous networks of solids and pores,[14] and it is an attractive candidate for ASCs as a positive electrode material. MoO$_2$ as a negative electrode was investigated because of its rich chemistry associated with multiple valence states, low electrical resistivity, natural

MOE Laboratory of Bioinorganic and Synthetic Chemistry, KLGHEI of Environment and Energy Chemistry, School of Chemistry and Chemical Engineering, Sun Yat-sen University, Guangzhou 510275, China. E-mail: ligaoren@mail.sysu.edu.cn

† Electronic supplementary information (ESI) available. See DOI: 10.1039/c5sc03326h

abundance, and affordable cost.[15] The unique helical hierarchical porous structure of Na_xMnO_2 was assembled from nanosheets and that of MoO_2 was assembled from mesoporous nanoparticles. The helix is a fantastic yet ubiquitous geometry in nature, science, art and architecture, and it exhibits distinctive mechanical, chemical, and physical properties.[16] When a helical structure is used in electrodes for supercapacitors, the appropriate spiral distance and diameter are in favor of electrolyte insertion and thus will improve the utilization ratio of the active material. The interspace between two pitches can serve as an "ion reservoir" and further improve the cycling stability of the electrodes. The hierarchical porous structure will be much less vulnerable to dissolution, Ostwald ripening and aggregation, and will provide a large surface area and fast electrolyte penetration/diffusion. Besides, the hierarchical porous structure can also buffer the volume change well, avoiding the structural collapse of the electrodes during the charge/discharge process. The electrochemical measurements demonstrate that the helical hierarchical porous Na_xMnO_2 shows a maximal areal capacitance of 329.69 mF cm^{-2} with a potential window of 0–1.0 V and the helical hierarchical porous MoO_2 shows a maximal areal C_{sp} of 174.97 mF cm^{-2} with a potential window of −1.1–0 V. The ASC device was assembled based on the helical hierarchical porous Na_xMnO_2/CC as the positive electrode and helical hierarchical porous MoO_2/CC as the negative electrode, and it shows a high volume C_{sp} of 2.04 F cm^{-3} and a high energy density of 0.92 mW h cm^{-3} based on the whole device. Meanwhile, such an ASC device exhibits a high cycling life with 97.22% C_{sp} retention after 6000 cycles. The present encouraging findings will open up a new opportunity for the development of ASCs with high energy and power densities.

2.   Experimental section

Preparation of electrode materials

All the chemical reagents used in this study were of analytical grade (AR). Electrodeposition was carried out in a simple two-electrode cell *via* galvanostatic electrolysis and a graphite electrode was used as a counter electrode (spectral grade). Carbon cloth was used as the working electrode for the electrodeposition and it was washed with ethanol and water successively in an ultrasonic bath for 5 min. The helical Na_xMnO_2 was electrodeposited on the carbon cloth in a 15 mL solution of 0.02 M $Mn(CH_3COO)_2$ + 0.2 M Na_2SO_4 at a current density of 4.0 mA cm^{-2} on the anode at room temperature for 10 min. The electrodeposition process is expressed as follows:[14,19]

$$Mn^{2+} + 2H_2O + xNa^+ \rightarrow Na_xMn_x^{3+}Mn_{(1-x)}^{4+}O_2 + 4H^+ + (2-x)e^- \qquad (1)$$
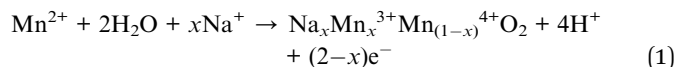
The helical MoO_2 was electrodeposited in a 15 mL solution of 0.01 M $(NH_4)_6Mo_7O_{24}$ at a current density of 4.0 mA cm^{-2} on the cathode at room temperature for 30 min followed by an annealing process in an NH_3 atmosphere. The electrodeposition process is expressed as follows:

$$6NH_4^+ + Mo_7O_{24}^{6-} + (18 - 7x)H_2O + (42 - 14x)e^- \rightarrow 7MoO_x + 6NH_3 + (42 - 14x)OH^- \qquad (2)$$
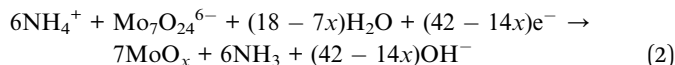
Fabrication of ASCs

The ASC device was assembled using the helical Na_xMnO_2/CC as the positive electrode and helical MoO_2/CC as the negative electrode with a separator (NKK separator; Nippon Kodoshi Corporation, Kochi, Japan) between the two electrodes. A Na_2SO_4 aqueous solution (1.0 M) was used as the electrolyte. To avoid leakage of the electrolyte, the entire device was sealed by two pieces of PET membrane with a small part of the electrode kept outside.

Material characterizations and electrochemical measurements

The morphologies, microstructures and compositions of the products were characterized using field-emission scanning electron microscopy (FE-SEM, JSM-6330F), X-ray diffraction (XRD, D-MAX 2200 VPC), transmission electron microscopy (TEM, Tecnai™ G2 F30), and X-ray photoelectron spectroscopy (XPS, ESCALab250). Inductively coupled plasma atomic emission spectroscopy (ICP, SPECTRO) was used to analyze the loading of the active materials. The electrochemical measurements of the electrodes were carried out in a standard three-electrode electrolytic cell in 1.0 M Na_2SO_4 aqueous solution. A graphite electrode was used as the counter electrode. A saturated calomel electrode (SCE) was used as the reference electrode. The cyclic voltammetry and chronopotentiometric measurements were performed using a CHI 760E electrochemical workstation (CH instruments, Inc.) to determine the electrochemical properties. EIS was conducted in the frequency range between 0.01 Hz and 100 kHz with an amplitude of 5 mV at the open-circuit potential.

3.   Results and discussion

As shown in Scheme 1, the electrodeposition method was used to fabricate the helical hierarchical porous Na_xMnO_2 and MoO_2, which were directly grown on carbon cloth without a binder (the details are described in the Experimental section). SEM images of Na_xMnO_2 with different magnifications are shown in Fig. 1a and S1a,† which show the perfect and uniform helical structures grown on carbon fibers. More interestingly, the magnified SEM image in Fig. 1b shows that the helical structures consist of nanosheets. The thickness of these nanosheets is 15–20 nm. TEM images of Na_xMnO_2 are shown in Fig. 1c and S1b,† which clearly show the porous structures. The HRTEM image in Fig. 1d shows the lattice spacings of 0.697, 0.349 and 0.252 nm, which correspond to (001), (002) and (100) crystal planes of Na_xMnO_2, respectively.[17] The SAED pattern in the inset of Fig. 1c also shows the polycrystalline structure of Na_xMnO_2. A cross-sectional SEM image in Fig. S2† shows that the thickness of the helical microstructures is ∼1.0 μm. The surface electronic state and chemical composition of the helical Na_xMnO_2 was

Scheme 1 Representation of the fabrication of the helical hierarchical porous Na$_x$MnO$_2$/CC and MoO$_2$/CC.

examined using an XPS spectrum. The XPS survey spectrum of the helical Na$_x$MnO$_2$ is shown in Fig. S3,† which shows the existence of the elements Mn, O, Na and C. The signals of C come from the carbon cloth substrate. The atomic ratio of Na/Mn is about 0.2, which is confirmed using energy dispersive X-ray spectroscopy (EDX) as shown in Fig. S4.† In the Mn 2p spectra (Fig. 1e), two kinds of manganese species containing Mn^{3+} and Mn^{4+} can be observed. The fitting peaks at 641.45 eV and 653.15 eV are indexed to Mn^{3+}, while the fitting peaks at 642.61 eV and 654.31 eV are indexed to Mn^{4+}.[18] Additionally, the Mn 3s peaks are useful for determining the oxidation state of

Mn. In Fig. 1f, the energy separation between the two peaks of Mn 3s is 4.8 eV, which corresponds to an average Mn oxidation state of ∼3.8 according to a linear relationship between the oxidation state of manganese and the ΔE value.[18,19] The atomic ratio of Mn^{3+}/Mn^{4+} in the sample is about 1/4. The O 1s spectrum shown in Fig. 1g is deconvoluted into three components. The bands at 529.9, 531.3 and 533.1 eV can be assigned to the oxygen bonds of Mn–O–Mn, Mn–O–H and H–O–H, respectively.[19] The bond of Mn–O–Mn comes from Na$_x$MnO$_2$ and those of Mn–O–H and H–O–H can be attributed to the adsorbed H$_2$O or crystal H$_2$O. Based on the above results, the composition of
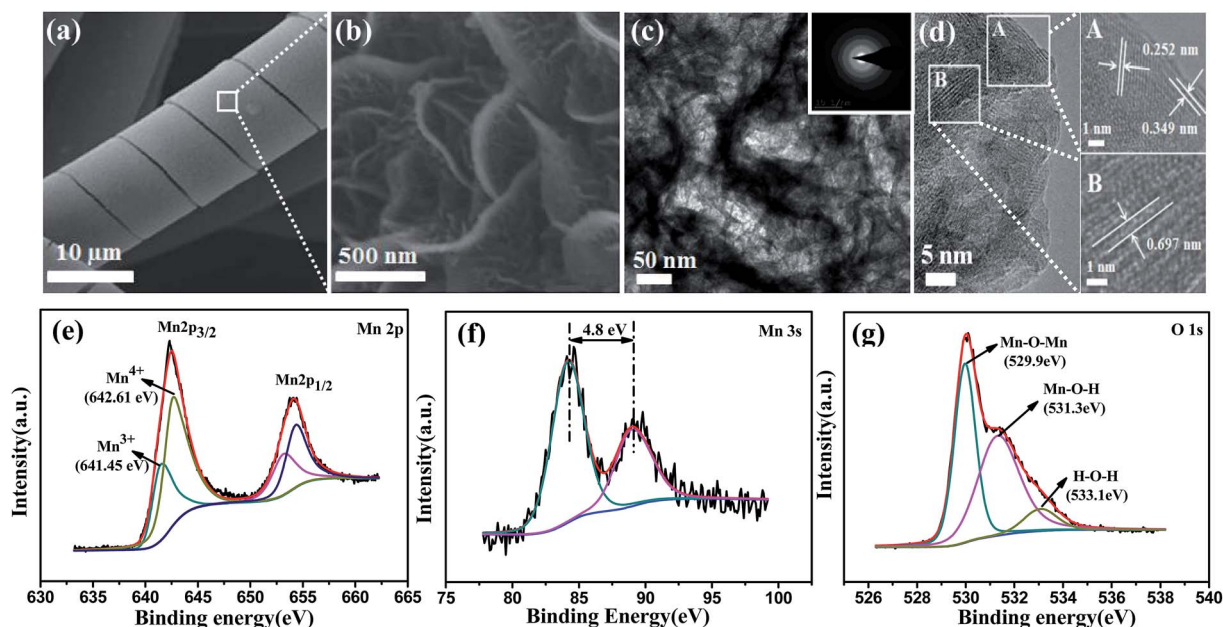

Fig. 1 (a and b) SEM images of the helical Na$_x$MnO$_2$ with hierarchical porous structures; (c) TEM and (d) HRTEM images of the typical Na$_x$MnO$_2$ nanosheets (inset in (c) is the SAED pattern); XPS spectra of the helical Na$_x$MnO$_2$ of (e) Mn 2p, (f) Mn 3s, and (g) O 1s.

the sodium–birnessite-type manganese oxide can be identified as $Na_{0.2}MnO_2$ ($Na_{0.2}Mn_{0.2}^{3+}Mn_{0.8}^{4+}O_2$).

Cyclic voltammetry (CV) and galvanostatic charge–discharge (GCD) are generally used to characterize the capacitance behavior of an electrode material. Fig. 2a and b show the typical CV and GCD curves of the helical Na_xMnO_2/CC at different scan rates and current densities, respectively, in 1.0 M Na_2SO_4 solution. In the potential range of 0–1.0 V, the behavior of the helical Na_xMnO_2/CC slightly deviates from the ideal rectangular shape with a small and broad redox couple, indicating the pseudocapacitance properties of the Na_xMnO_2/CC. These redox peaks can be definitely ascribed to the intercalation–deintercalation of Na^+ into and from the solid MnO_2 lattice.[14,19,20] The GCD curves of the helical Na_xMnO_2/CC are almost linear and symmetrical without an obvious IR drop as shown in Fig. 2b, indicating a rapid I–V response and a good capacitance performance. The areal C_{sp} of the helical Na_xMnO_2/CC obtained from the GCD curves is shown in Fig. 2c, which shows that the highest C_{sp} is 329.69 mF cm^{-2} at a current density of 0.29 mA cm^{-2}. The C_{sp} value of 329.69 mF cm^{-2} is much higher than those of the other MnO_2 electrodes reported in the literature (10–100 mF cm^{-2}).[4,21] In addition, the helical Na_xMnO_2/CC electrode has a small charge-transfer resistance (R_{ct}) of ∼1.5 Ω as shown in Fig. 2d, suggesting fast charge transfer and transport processes.[22] Fig. S7† shows the excellent cycling stability of the helical Na_xMnO_2/CC and a high C_{sp} retention of 99.97% after 5000 cycles is achieved. In addition, Fig. S8† shows the EIS spectra of the helical Na_xMnO_2/CC before and after 5000 cycles, from which we can see that the charge-transfer resistance is almost unchanged after 5000 cycles.

The helical MoO_2/CC as a negative electrode was fabricated as shown in Fig. 3a. The helical structure is constructed by nanoparticles with diameters of 100–200 nm as shown in Fig. 3b and S9a.† A TEM image of MoO_2 is shown in Fig. S9b,† which clearly shows the porous structures. The thickness of the helical structure is ∼3.5 μm as shown in Fig. S9a.† More importantly, the magnified TEM shows these nanoparticles are mesoporous as shown in Fig. 3c, which will be beneficial to enhance the specific surface area and thus will provide more active reaction sites. Fig. 3d shows the HRTEM image of the helical MoO_2, in which the lattice spacings of 0.243, 0.240, 0.171 and 0.170 nm correspond to (−211), (−202), (−312) and (−222) crystal planes of MoO_2 (JCPDS#32-0671), respectively.[23] The SAED pattern in the inset of Fig. 3c reveals the diffraction rings of the typical monoclinic structure of MoO_2, which is in accordance with the results from the XRD pattern shown in Fig. 3e. All diffraction peaks can be assigned to the monoclinic MoO_2 phase and no diffraction peak comes from other molybdenum oxides such as MoO_3. The survey XPS spectra of the MoO_2 electrode is shown in Fig. S10,† which indicates the presence of Mo, O and C elements in the sample. The atomic ratio of Mo/O is about 2, which is consistent with stoichiometric MoO_2 composition. The elemental C comes from the carbon cloth that is used as the substrate. The high-resolution XPS spectrum of Mo 3d can be deconvoluted into two doublets as shown in Fig. 3f. The binding energies of the Mo $3d_{5/2}$ and $3d_{3/2}$ peaks at 229.6 and 232.9 eV indicate the oxidation state of Mo(IV).[24] In addition, the small peaks at 232.5 and 235.6 eV are seen, and they correspond to Mo(VI) $3d_{5/2}$ and $3d_{3/2}$, respectively, indicating the existence of Mo(VI). This can be attributed to the partial surface oxidation of
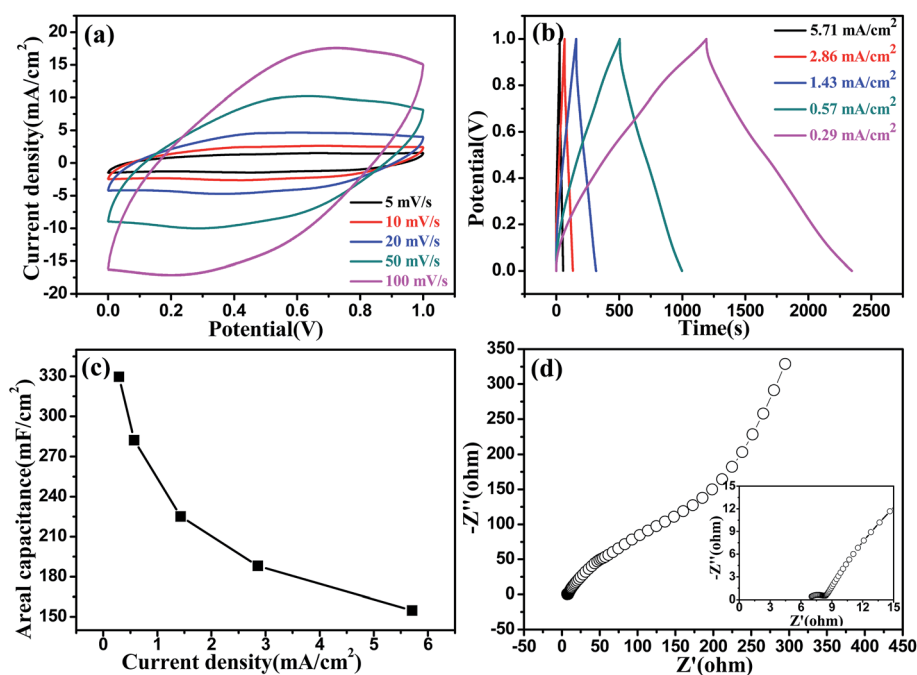

Fig. 2 (a) CV curves of the helical Na_xMnO_2 at different scan rates; (b) GCD curves of the helical Na_xMnO_2 at different current densities in 1.0 M Na_2SO_4 electrolyte; (c) areal capacitance calculated from GCD curves as a function of current densities; (d) EIS spectra of the Na_xMnO_2 (inset is the enlarged view of the high frequency region).
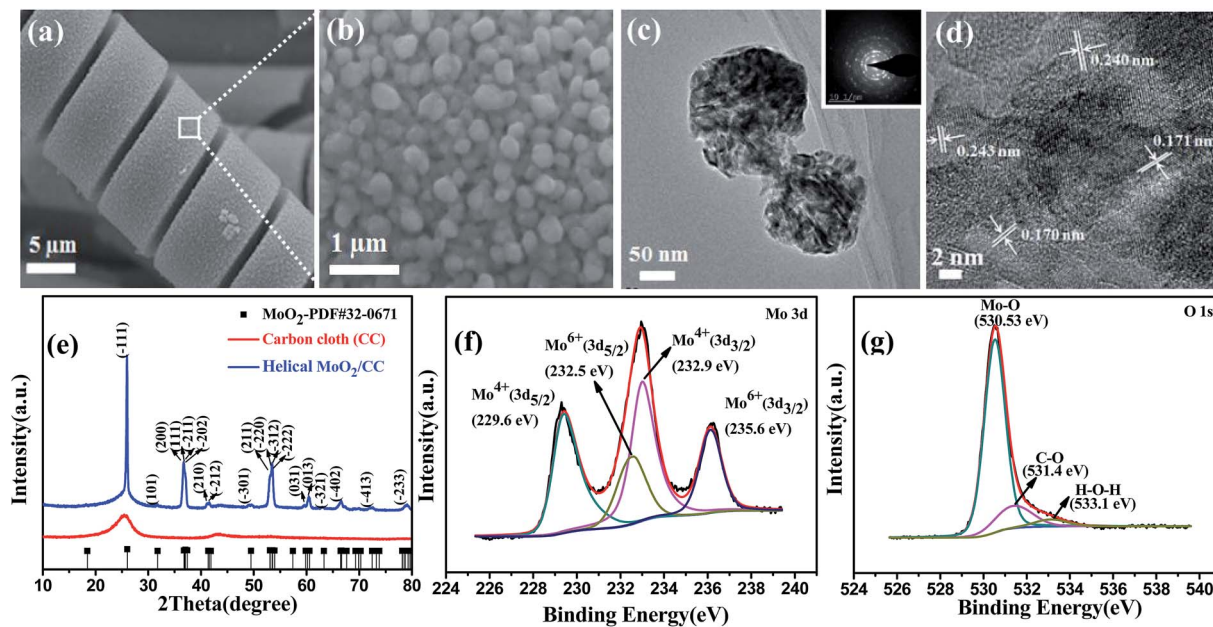
Fig. 3 (a and b) SEM images of the helical MoO_2 with different magnifications; (c) the TEM image of MoO_2 nanoparticles (inset is the SAED pattern); (d) the HRTEM image of the helical MoO_2; (e) XRD patterns of the helical MoO_2/CC and CC; XPS spectra of the helical MoO_2/CC: (f) Mo 3d and (g) O 1s.

MoO_2 in air.[24,25] The XPS spectrum of O 1s is shown in Fig. 3g, which shows that the main peak at 530.53 eV can be assigned to the Mo–O bond. The bands of 531.4 and 533.1 eV correspond to C–O and O–H bonds, respectively,[24,25] and they can be attributed to the adsorbed H_2O on the carbon cloth.

The fabricated helical MoO_2/CC electrode possesses a perfect capacitance behavior with a wide potential window of −1.1–0 V (vs. SCE) in a solution of 1.0 M Na_2SO_4. The wide potential window may be the result of the high overpotential of H_2 and O_2 evolution, which is related to the structure and properties of the electrode material.[26] Fig. 4a and b show the CV and GCD curves of the helical MoO_2/CC, respectively, which are symmetric and linear, respectively, without an obvious IR drop, indicating a good capacitance performance. As shown in Fig. 4c, the highest areal C_{sp} obtained from the GCD curves is 174.97 mF cm^{-2} at a current density of 1.43 mA cm^{-2}, which is much larger than those of other metal oxide/nitride negative electrodes, such as α-Fe_2O_3,[27] MoO_3,[28a] and VN.[12a,28b] The kinetic features of the helical MoO_2/CC electrode were further investigated by measuring the EIS spectrum as shown in Fig. 4d, which shows a small bulk solution resistance (R_s) of 7.5 Ω,[29] a small charge-transfer resistance (R_{ct}) of 0.5 Ω, and fast ion diffusion into the MoO_2/CC electrode.[30] Moreover, the helical MoO_2/CC shows a high cycling stability with a C_{sp} retention of 91.62% after 5000 cycles as shown in Fig. S12.† To evaluate the change of charge-transfer resistance, we compared the EIS spectra of the helical MoO_2/CC before and after the cycling test as shown in Fig. S13,† from which we can see that the charge-transfer resistance of the electrode becomes a little bigger after 5000 cycles.

The flexible asymmetric supercapacitor (ASC) device was assembled using the helical Na_xMnO_2/CC as the positive electrode and the helical MoO_2/CC as the negative electrode (Na_xMnO_2/CC//MoO_2/CC ASC). Fig. 5a shows the schematic structure of the Na_xMnO_2/CC//MoO_2/CC ASC, which is sealed by two thin pieces of PET membrane. Taking advantage of the different potential windows of the Na_xMnO_2/CC and MoO_2/CC electrodes (Fig. S14a†), the operating cell potential of the assembled ASCs is expected to be 2.1 V. However, a faradic reaction is observed in the CV and GCD curves beyond the potential of 1.8 V. As shown in Fig. S14b,† an oxidation peak is observed beyond 1.8 V, highlighted by a dashed box, which is also observed in the GCD curves (Fig. S14c†). When the ASC devices were tested in the potential windows of 2.0 and 2.1 V for 6000 cycles, their capacitance retention is only 63.01% and 40.25%, respectively, as shown in Fig. S14d.† However, when tested in a potential window of 1.8 V, the ASC has a good cycling stability with a much higher capacitance retention of 97.22%, which is significantly better than those reported in previous work (typically 70–85% retention over 1000 cycles).[26a,32]

Fig. 5b shows the CV curves of an optimized Na_xMnO_2/CC//MoO_2/CC ASC at different scan rates with a potential window of 0–1.8 V in 1.0 M Na_2SO_4 electrolyte. These CV curves exhibit rectangular-like shapes, revealing an ideal capacitive behavior and fast charge/discharge properties. As shown in Fig. 5c, the GCD curves at different current densities are all reasonably symmetrical and show a good linear relationship of the charge/discharge voltage versus time particularly at a low current density. This result also indicates the ideal capacitive characteristics and the rapid charge/discharge properties of the assembled ASC device. The volumetric C_{sp} calculated using the discharging curves is shown in Fig. S15,† which shows the highest C_{sp} of 2.04 F cm^{-3} at 0.57 mA cm^{-2}. The C_{sp} of 2.04 F cm^{-3}

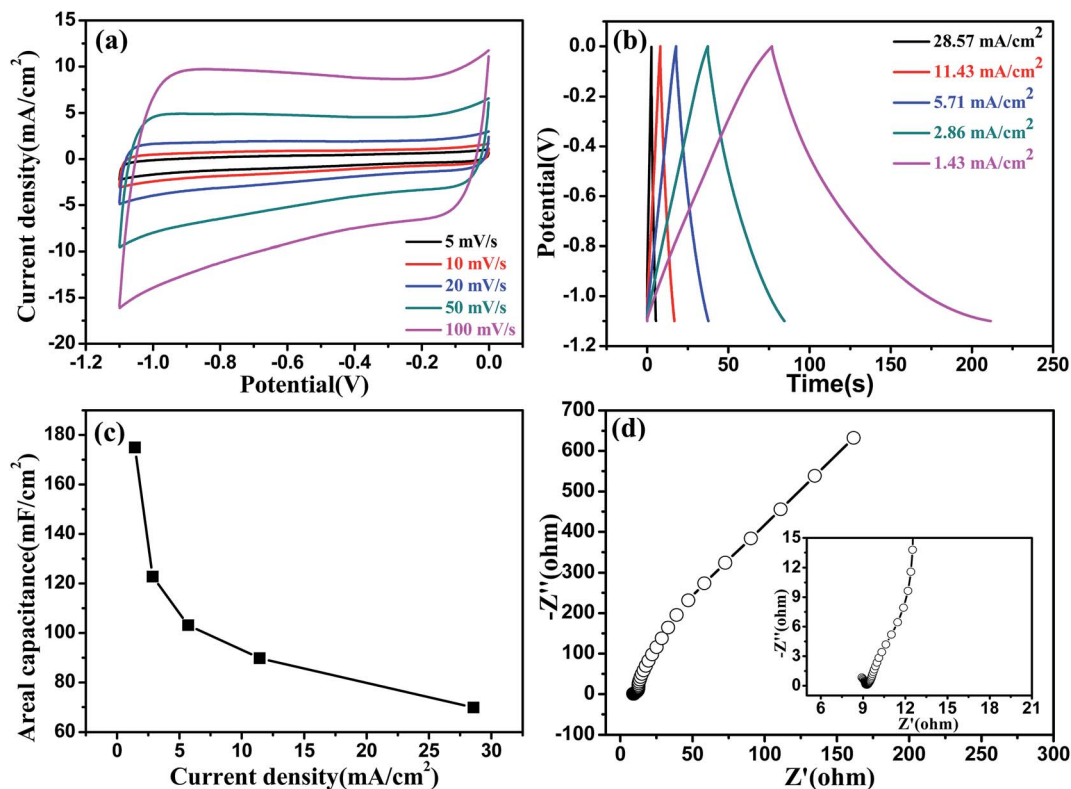**Fig. 4** (a) CV curves at different scan rates; (b) GCD curves at different current densities of the helical MoO_2 in 1.0 M Na_2SO_4 electrolyte; (c) areal capacitance calculated from GCD curves as a function of current densities; (d) EIS spectra of MoO_2 (inset is the enlarged view of the high frequency region).
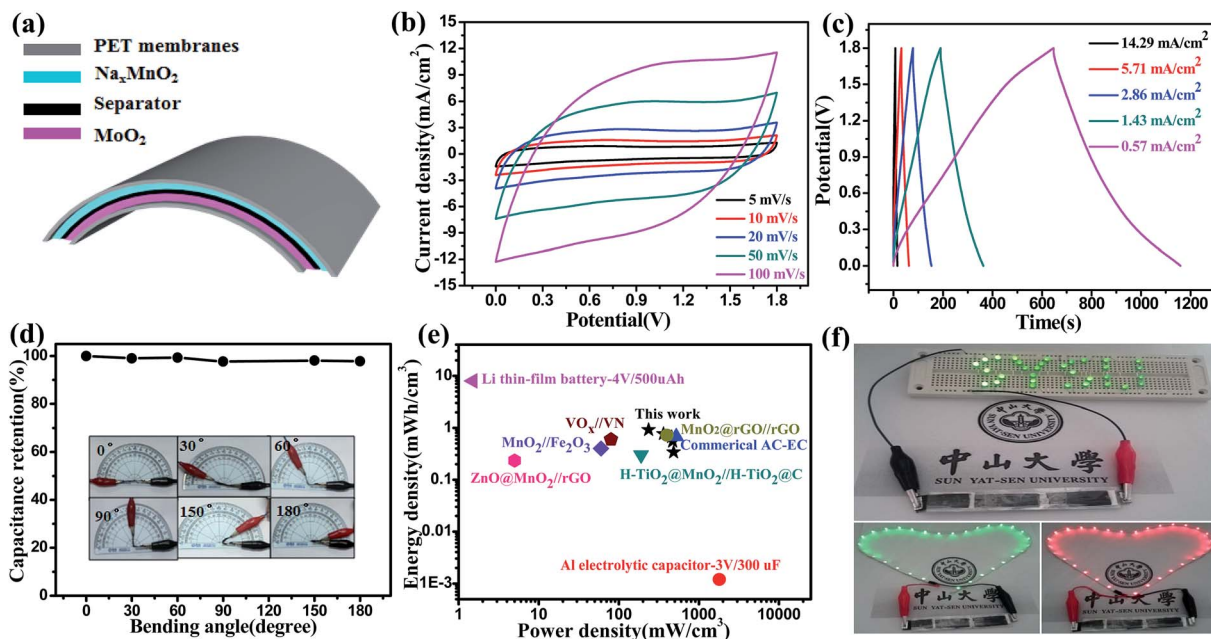

Fig. 5 (a) A schematic illustration of the structure of a flexible Na_xMnO_2/CC//MoO_2/CC ASC with two electrodes separated by the TF45 (NKK) membrane (separator); (b) CV curves of the ASC at different scan rates; (c) GCD curves of the ASC at different current densities; (d) stability performance of the ASC collected at different bending angles (the inset shows the flexibility under the different bending angles); (e) Ragone plots of the Na_xMnO_2/CC//MoO_2/CC ASC device. The values reported in the literature for other ASC devices are added for comparison; (f) a SYSU logo consisting of 32 green LEDs and a piece of commercial red or green LED soft rope light powered by the assembled ASCs with three in series.

is much larger than those of the ASCs reported recently.[4,11a,12a,31] In order to demonstrate the flexibility, we measured the CV curves of the assembled ASCs with different bending angles from 0° to 180° at a scan rate of 100 mV s^{-1}. As shown in Fig. 5d and S16,† there is no significant C_{sp} loss under the different bending angles, suggesting excellent flexibility properties.

The flexible $Na_xMnO_2/CC//MoO_2/CC$ ASC exhibits the highest energy density of 0.92 mW h cm^{-3} at a power density of 236.15 mW cm^{-3} as shown in Fig. 5e. It preserves 36.96% of the highest energy density when the power density increases to the maximal value (483.19 mW cm^{-3}). Here the energy densities are superior to those of the previously reported similar ASC systems, including $MnO_2//Fe_2O_3$ (1.6 V, 0.40 mW h cm^{-3}),[11a] H–$TiO_2@MnO_2//H–TiO_2@C$ (1.8 V, 0.30 mW h cm^{-3}),[4] $ZnO@MnO_2/rGO$ (1.8 V, 0.234 mW h cm^{-3}),[6] and even $VO_x//VN$ (1.8 V, 0.61 mW h cm^{-3}).[12a] To show the practical application, three ASC devices were assembled in series. As shown in Fig. 5f, the ASCs can light a SYSU logo consisting of 32 green LEDs and a 50 cm long commercial red (2.0 V) and green (2.5 V) LED soft rope light, indicating high power and energy densities of the $Na_xMnO_2/CC//MoO_2/CC$ ASCs.

4. Conclusions

In summary, we pioneered an electrochemical method for the synthesis of helical Na_xMnO_2/CC and MoO_2/CC with hierarchical porous structures, which are assembled from nanosheets and mesoporous nanoparticles, respectively. These unique electrode structures enable a high working voltage in aqueous solutions, a high areal capacitance and an outstanding cycling performance. High-performance $Na_xMnO_2/CC//MoO_2/CC$ ASCs based on the helical Na_xMnO_2/CC as the positive electrodes and the helical MoO_2/CC as the negative electrodes are assembled, and they achieve a maximum volume C_{sp} of 2.04 F cm^{-3} and a maximum energy density of 0.92 mW h cm^{-3} based on the whole device. Furthermore, the $Na_xMnO_2/CC//MoO_2/CC$ ASCs exhibit an excellent cycling stability with 97.22% capacitance retention after 6000 cycles. These findings will open new opportunities for the development of helical hierarchical porous metal oxide electrodes for ASC devices with high energy and power densities.

Acknowledgements

References

1 (a) C. Liu, F. Li, L. P. Ma and H. M. Cheng, *Adv. Mater.*, 2010, **22**, 28; (b) G. Yu, L. Hu, M. Vosgueritchian, H. Wang, X. Xie, J. R. McDonough, X. Cui, Y. Cui and Z. Bao, *Nano Lett.*, 2011, **11**, 2905; (c) H. Xia, C. Hong, B. Li, B. Zhao, Z. Lin, M. Zheng, S. V. Savilov and S. M. Aldoshin, *Adv. Funct. Mater.*, 2015, **25**, 627.

2 (a) P. Simon and Y. Gogotsi, *Nat. Mater.*, 2008, **7**, 845; (b) J. R. Miller and P. Simon, *Science*, 2008, **321**, 651; (c) R. Liu, F. Wong, W. Duan and A. Sen, *Adv. Mater.*, 2013, **25**, 6997; (d) C. Zhu, P. Yang, D. Chao, X. Wang, X. Zhang, S. Chen, B. K. Tay, H. Huang, H. Zhang, W. Mai and H. J. Fan, *Adv. Mater.*, 2015, **27**, 4566; (e) G. D. Moon, J. B. Joo, M. Dahl, H. Jung and Y. Yin, *Adv. Funct. Mater.*, 2014, **24**, 848.

3 (a) J. Chang, M. Jin, F. Yao, T. H. Kim, V. T. Le, H. Yue, F. Gunes, B. Li, A. Ghosh, S. Xie and Y. H. Lee, *Adv. Funct. Mater.*, 2013, **23**, 5074; (b) P. J. Hall, M. Mirzaeian, S. I. Fletcher, F. B. Sillars, A. J. R. Rennie, G. O. Shitta-Bey, G. Wilson, A. Cruden and R. Carter, *Energy Environ. Sci.*, 2010, **3**, 1238; (c) J. Feng, X. Sun, C. Wu, L. Peng, C. Lin, S. Hu, J. Yang and Y. Xie, *J. Am. Chem. Soc.*, 2011, **133**, 17832.

4 (a) X. Lu, M. Yu, G. Wang, T. Zhai, S. Xie, Y. Ling, Y. Tong and Y. Li, *Adv. Mater.*, 2013, **25**, 267; (b) C. Wu, X. Lu, L. Peng, K. Xu, X. Peng, J. Huang, G. Yu and Y. Xie, *Nat. Commun.*, 2013, **4**, 2431; (c) H. Xia, C. Hong, X. Shi, B. Li, G. Yuan, Q. Yao and J. Xie, *J. Mater. Chem. A*, 2015, **3**, 1216; (d) D. Chao, X. Xia, C. Zhu, J. Wang, J. Liu, J. Lin, Z. Shen and H. J. Fan, *Nanocale*, 2014, **6**, 5691–5697.

5 (a) X. Lu, M. Yu, G. Wang, Y. Tong and Y. Li, *Energy Environ. Sci.*, 2014, **7**, 2160; (b) J.-X. Feng, S.-H. Ye, A.-L. Wang, X.-F. Lu, Y.-X. Tong and G.-R. Li, *Adv. Funct. Mater.*, 2014, **24**, 7093; (c) C. Zhou, Y. Zhang, Y. Li and J. Liu, *Nano Lett.*, 2013, **13**, 2078.

6 W. Zilong, Z. Zhu, J. Qiu and S. Yang, *J. Mater. Chem. C*, 2014, **2**, 1331.

7 M. Yu, W. Wang, C. Li, T. Zhai, X. Lu and Y. Tong, *NPG Asia Mater.*, 2014, **6**, 129.

8 X. F. Lu, D. J. Wu, R. Z. Li, Q. Li, S. H. Ye, Y. X. Tong and G. R. Li, *J. Mater. Chem. A*, 2014, **2**, 4706.

9 (a) L. Liu, Z. Niu, L. Zhang, W. Zhou, X. Chen and S. Xie, *Adv. Mater.*, 2014, **26**, 4855–4862; (b) L. Dai, D. W. Chang, J. B. Baek and W. Lu, *Small*, 2012, **8**, 1130.

10 G. R. Li, Z. L. Wang, F. L. Zheng, Y. N. Ou and Y. X. Tong, *J. Mater. Chem.*, 2011, **21**, 4217.

11 (a) X. Lu, Y. Zeng, M. Yu, T. Zhai, C. Liang, S. Xie, M. S. Balogun and Y. Tong, *Adv. Mater.*, 2014, **26**, 3148; (b) P. Yang, Y. Ding, Z. Lin, Z. Chen, Y. Li, P. Qiang, M. Ebrahimi, W. Mai, C. P. Wong and Z. L. Wang, *Nano Lett.*, 2014, **14**, 731.

12 (a) X. Lu, M. Yu, T. Zhai, G. Wang, S. Xie, T. Liu, C. Liang, Y. Tong and Y. Li, *Nano Lett.*, 2013, **13**, 2628; (b) K.-H. Lee, Y.-W. Lee, A. R. Ko, G. Cao, K.-W. Park and B. Vyas, *J. Am. Ceram. Soc.*, 2013, **96**, 37.

13 (a) Q. Li, Z.-L. Wang, G.-R. Li, L.-X. Ding and Y.-X. Tong, *Nano Lett.*, 2012, **12**, 3803; (b) Z.-P. Feng, G.-R. Li, J.-H. Zhong,

Z.-L. Wang, Y.-N. Ou and Y.-X. Tong, *Electrochem. Commun.*, 2009, **11**, 706.

14 L. Athouel, F. Moser, R. Dugas, O. Crosnier, D. Belanger and T. Brousse, *J. Phys. Chem. C*, 2008, **112**, 7270.

15 (*a*) K. M. Hercule, Q. Wei, A. M. Khan, Y. Zhao, X. Tian and L. Mai, *Nano Lett.*, 2013, **13**, 5685; (*b*) H.-J. Zhang, T.-H. Wu, K.-X. Wang, X.-Y. Wu, X.-T. Chen, Y.-M. Jiang, X. Wei and J.-S. Chen, *J. Mater. Chem. A*, 2013, **1**, 12038.

16 Z. Ren and P. X. Gao, *Nanoscale*, 2014, **6**, 9366.

17 H. Kanoh, W. Tang, Y. Makita and K. Ooi, *Langmuir*, 1997, **13**, 6845–6849.

18 S. R. Das, I. R. Fachini, S. B. Majumder and R. S. Katiyar, *J. Power Sources*, 2006, **158**, 518.

19 M. Nakayama, S. Konishi, H. Tagashira and K. Ogura, *Langmuir*, 2005, **21**, 354.

20 (*a*) Q. T. Qu, Y. Shi, S. Tian, Y. H. Chen, Y. P. Wu and R. Holze, *J. Power Sources*, 2009, **194**, 1222; (*b*) Y. K. Zhou, M. Toupin, D. Bélanger, T. Brousse and F. Favier, *J. Phys. Chem. Solids*, 2006, **67**, 1351; (*c*) M. Nakayama and H. Tagashira, *Langmuir*, 2006, **22**, 3864.

21 (*a*) Y. Huang, Y. Li, Z. Hu, G. Wei, J. Guo and J. Liu, *J. Mater. Chem. A*, 2013, **1**, 9809; (*b*) S. W. Lee, J. Kim, S. Chen, P. T. Hammond and Y. Shao-Horn, *ACS Nano*, 2010, **4**, 3889.

22 P. Justin, S. K. Meher and G. R. Rao, *J. Phys. Chem. C*, 2010, **114**, 5203.

23 (*a*) L. C. Yang, Q. S. Gao, Y. Tang, Y. P. Wu and R. Holze, *J. Power Sources*, 2008, **179**, 357; (*b*) X. Zhao, M. Cao, B. Liu, Y. Tian and C. Hu, *J. Mater. Chem.*, 2012, **22**, 13334.

24 (*a*) Q. Qu, T. Gao, H. Zheng, Y. Wang, X. Li, X. Li, J. Chen, Y. Han, J. Shao and H. Zheng, *Adv. Mater. Interfaces*, 2015, **2**, DOI: 10.1002/admi.201500048; (*b*) Y. Sun, X. Hu, W. Luo and Y. Huang, *ACS Nano*, 2011, **5**, 7100.

25 K. Zhou, W. Zhou, X. Liu, Y. Sang, S. Ji, W. Li, J. Lu, L. Li, W. Niu, H. Liu and S. Chen, *Nano Energy*, 2015, **12**, 510.

26 (*a*) Z. S. Wu, W. Ren, D. W. Wang, F. Li, B. Liu and H. M. Cheng, *ACS Nano*, 2010, **4**, 5835; (*b*) C. Xu, H. Du, B. Li, F. Kang and Y. Zeng, *J. Electrochem. Soc.*, 2009, **156**, 435.

27 (*a*) S. Shivakumara, T. R. Penki and N. Munichandraiah, *ECS Electrochem. Lett.*, 2013, **2**, 60; (*b*) K. K. Lee, S. Deng, H. M. Fan, S. Mhaisalkar, H. R. Tan, E. S. Tok, K. P. Loh, W. S. Chin and C. H. Sow, *Nanoscale*, 2012, **4**, 2958.

28 (*a*) Y. Liu, B. Zhang, Y. Yang, Z. Chang, Z. Wen and Y. Wu, *J. Mater. Chem. A*, 2013, **1**, 13582; (*b*) P. Jampani, A. Manivannan and P. N. Kumta, *Electrochem. Soc. Interface*, 2010, **19**, 57.

29 (*a*) R. Rakhi, W. Chen, D. Cha and H. Alshareef, *Nano Lett.*, 2012, **12**, 2559; (*b*) G. Zhang, W. Li, K. Xie, F. Yu and H. Huang, *Adv. Funct. Mater.*, 2013, **23**, 3675.

30 L. Li, Y. Cheah, Y. Ko, P. Teh, G. Wee, C. Wong, S. Peng and M. Srinivasan, *J. Mater. Chem.A*, 2013, **1**, 10935.

31 X. Lu, G. Wang, T. Zhai, M. Yu, S. Xie, Y. Ling, C. Liang, Y. Tong and Y. Li, *Nano Lett.*, 2012, **12**, 5376.

32 S. Chen, J. Zhu, X. Wu, Q. Han and X. Wang, *ACS Nano*, 2010, **4**, 2822.